RSC Advances

PAPER

View Article Online
View Journal | View Issue

Cite this: *RSC Adv.*, 2023, **13**, 10884

Admirable stability achieved by ns^2 ions Co-doping for all-inorganic metal halides towards optical anti-counterfeiting†

Chuang Yang,[a] Fengwan Guo,*[ab] Shanping Wang,[a] Wenwen Chen,[a] Yu Zhang,[a] Nan Wang,[a] Zhuozhen Li[a] and Juan Wang *[ac]

Optical materials play a momentous role in anti-counterfeiting field, such as authentication, currency and security. The development of tunable optical properties and optical responses to a range of external stimuli is quite imperative for the growing demand of optical anti-counterfeiting technology. Metal halide perovskites have attracted much attention of researchers due to their excellent optical properties. In addition, co-doping methods have been gradually applied to the research of metal halide perovskites, by which more abundant luminescence phenomena can be introduced into the host perovskite. Herein, the ns^2 ions of bismuth (Bi^{3+}) and antimony (Sb^{3+}) ions co-doped zero-dimensional Cs_2SnCl_6 metal halide with an excitation-wavelength-dependent emission phenomenon is synthesized as an efficient multimodal luminescent material, the luminescence of which is tunable and covers a wide region of color. What's more, a dynamic dual-emission phenomenon is captured when the excitation wavelength changes from 320 nm to 420 nm for Cs_2SnCl_6:$Bi_{0.08}Sb_{0.12}$ crystals. Moreover, the Bi^{3+} and Sb^{3+} doped metal halide material shows great enhancement in solvent resistance and thermal stability compared to the pristine Cs_2SnCl_6. The admirable stability and distinguishable photoluminescence (PL) phenomenon of this all-inorganic metal halide has great potential to be applied in optical anti-counterfeiting technology. Furthermore, the co-doping method can accelerate the discovery of new luminescence phenomena in original metal halide perovskites.

Received 17th January 2023
Accepted 23rd March 2023

DOI: 10.1039/d3ra00351e

rsc.li/rsc-advances

Introduction

Nowadays, counterfeit products have penetrated into plenty of industries, such as digital, food, clothing and so on, which is a widespread and disturbing phenomenon in our daily life.[1] Optical materials offer the advantages of visibility, high throughput, and facile design and are widely applied in the anti-counterfeiting field.[2–6] However, in traditional fluorescent anti-counterfeiting techniques, monochromatic fluorescent phosphors are generally used.[7,8] This is still unsafe because monochromatic fluorescence can be easily achieved by other fluorescent materials. Therefore, the development of polychromatic fluorescence anti-counterfeiting technology is urgent to meet our practical demands. To solve this problem, organic and rare earth materials with abundant fluorescence are applied into anti-counterfeiting field to achieve excitation-wavelength-dependent fluorescent colors.[4,9–11] But the poor stability of organic material and the lack of rare earth material might limit their further development. Therefore, single component and tunable fluorescent material with high stability are in great demand in the practical application.[12]

Due to excellent optical properties, metal halide perovskite has attracted much attention of researchers.[13–15] Among them, lead halide perovskite owns particularly outstanding performance. However, the toxicity and instability of lead perovskite restrict its development steps.[16,17] As well as looking for lead replacements, the researchers also altered the optical properties by reducing the dimension of perovskite.[18–21] For the fact that lower dimensionality seems more probable to lead octahedral distortion and STEs formation, attempts on lower dimensional metal halides is increasing rapidly in this era of intense scientific research, especially for 0 dimensional metal halides.[22–25]

Cs_2SnX_6 (X = Cl, Br, I) nanocrystals have been investigated for its tunable light emission and photocatalytic activity.[26–31] What's more, mixed halide $Cs_2SnCl_{6-x}Br_x$ single crystals have been successfully applied into narrowband photodetection.[32]

[a]*Collaborative Innovation Center for Advanced Organic Chemical Materials, Co-constructed by the Province and Ministry of Education Key Laboratory for the Synthesis and Application of Organic Functional Molecules, College of Chemistry and Chemical Engineering, Hubei University, Wuhan 430062, P. R. China. E-mail: fwg@pku.edu.cn; wangjuan_hd@163.com*

[b]*Hubei Key Laboratory of Ferro & Piezoelectric Materials and Devices, Hubei University, Wuhan, 430062, P. R. China*

[c]*Collaborative Innovation Center for Advanced Organic Chemical Materials Co-constructed by the Province and Ministry, Hubei University, Wuhan, 43006, P. R. China*

† Electronic supplementary information (ESI) available. See DOI: https://doi.org/10.1039/d3ra00351e

Doping methods have also been applied to the research of Cs_2SnCl_6 crystals/nanocrystals. Tang'group reported bismuth-doped Cs_2SnCl_6 crystals as blue emissive phosphors.[33] Later, Xia'group reported antimony-doped Cs_2SnCl_6 nanocrystals which realized broad-band emission.[34] Liu'group realized Bi/Sb doped Cs_2SnCl_6 separately and tune visible emission of Cs_2SnCl_6:Bi and Cs_2SnCl_6:Sb phosphors by changing post-annealing temperature.[35] This development opens up new opportunities for these materials as candidates for solid state lighting. On the other hand, the method of multi-ion co-doping has been gradually applied to the research of metal halide perovskite, by which more abundant luminescence phenomenon can be introduced into the host perovskite.[36] Xu's group synthesized Mn^{2+} and Sb^{3+} co-doped $Cs_2NaInCl_6$ nanocrystals, displaying adjustable and continuous luminescence.[37] Chen's group achieved dual-band-tunable white-light emission in Cs_2SnCl_6 by co-doping Bi^{3+} and Te^{4+}.[38] The Bi^{3+} and Sb^{3+} codoped Cs_2SnCl_6 system has also been reported.[39] However, the dynamic dual emission phenomenon of the co-doping system and its related application prospects remain to be explored. Herein, we synthesized a series of lead-free zero-dimensional Cs_2SnCl_6:$Bi_{0.2-x}Sb_x$ (x = 0, 0.04, 0.08, 0.12, 0.16, 0.2) metal halides crystals by doping Bi^{3+} and Sb^{3+} simultaneously, from which there is an interesting excitation-wavelength-dependent phenomenon. The PL intensity will change not only by the dopant content, but also by the different excitation wavelength. The impurity ions doped metal halide material shows an enhancement in PLQY about 40% compared to the pristine Cs_2SnCl_6 where there is no PL phenomenon being observed under the UV light. The UV-vis spectrum, X-ray photoelectron spectroscopy (XPS) and Raman spectrum were applied to investigate the effect of Bi and Sb co-doping on properties of Cs_2SnCl_6 metal halide crystals. The variable excitation wavelength PL spectrum and the time-resolved photoluminescence (TRPL) spectrum are used to study the dual-emission phenomenon. With excellent stability against air, high temperature and organic solvents, the Cs_2SnCl_6:$Bi_{0.2-x}Sb_x$ metal halide material has great potential to become anti-counterfeiting material.

Results and discussion

The zero-dimensional Cs_2SnCl_6 metal halide crystals are almost transparent under ambient, which are crystallized in the space group cubic $Fm\bar{3}m$. The tin cation(IV) is coordinated with six chloride anions, constructing a $[SnCl_6]^{2-}$ octahedron. Each $[SnCl_6]^{2-}$ octahedron is separated by Cs^+, which owns large radius, forming a typical zero-dimensional structure (Fig. 1a). The powder X-ray diffraction (PXRD) in Fig. 1b shows the Cs_2SnCl_6:$Bi_{0.2-x}Sb_x$ crystals can well correspond to pure Cs_2SnCl_6 phase, indicating that the Bi^{3+} and Sb^{3+} co-doping has little influence in the host crystal structure.

In Fig. 1c, The PXRD peaks of impurity doping sample exhibit varying degrees shift compared to the pristine sample, which suggest that the Bi^{3+} and Sb^{3+} cations are incorporated into the host crystal lattice successfully. For the fact that the radius of Bi^{3+} (1.03 Å) and Sb^{3+} (0.90 Å) are bigger than the

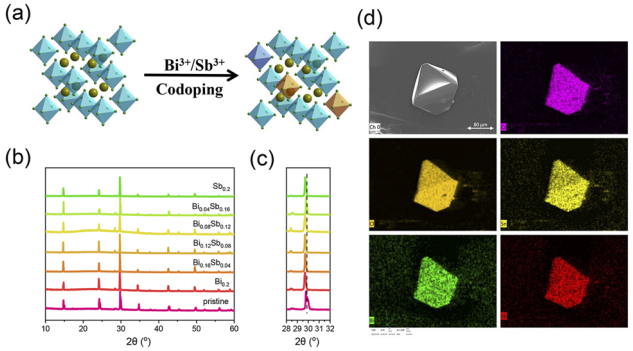

Fig. 1 (a) The diagram of Bi^{3+}/Sb^{3+} co-doping in zero-dimensional Cs_2SnCl_6 metal halides (Sn cyan, Cs dark yellow, Cl green, Bi light blue, Sb light orange). Full range (b) and selected range (c) of the PXRD pattern of measured data for Cs_2SnCl_6:$Bi_{0.2-x}Sb_x$ (x = 0.04, 0.08, 0.12, 0.16, 0.2) sample. (d) The SEM image and EDS mapping of Cs_2SnCl_6:$Bi_{0.08}Sb_{0.12}$.

radius of Sn^{4+} (0.71 Å), the peak of PXRD shifts to a lower angle when impurity doping due to the lattice expansion.[40–42] The field emission scanning electron microscope (FESEM) image (Fig. 1d) shows that the crystals possess excellent crystal morphology, which shows the high crystallinity. The energy dispersive X-ray spectrometry (EDS) mapping was performed to verify the composition of the Cs_2SnCl_6:$Bi_{0.08}Sb_{0.12}$ sample by collecting Cs, Sn, Cl, Bi, and Sb signatures. As shown in Fig. 1d, these five elements are evenly distributed over grains and perfectly covered each other, demonstrating the uniform composition of the crystals.[43] In order to understand the actual doping amount of impurity ions, we carry out ICP-MS test on the codoped crystals. The result of ICP-MS is showed in Table S1.† From the Table S1,† we can find that the Bi^{3+} and Sb^{3+} in precursor were only partially incorporated into the products. But for the sake of expression, we still use the original formula.

In Fig. 2, there are the pictures of pristine Cs_2SnCl_6 and Cs_2SnCl_6:$Bi_{0.2-x}Sb_x$ (x = 0, 0.04, 0.08, 0.12, 0.16, 0.2) crystals irradiated by a UV lamp at 365 nm and 395 nm. The PL of Cs_2SnCl_6:$Bi_{0.2-x}Sb_x$ changes between blue, purple and red. Fig. 3 shows the PLE and PL spectrum of different co-doping Bi^{3+}/Sb^{3+} content of Cs_2SnCl_6 at the excitation wavelength of 365 nm and 395 nm. The pristine Cs_2SnCl_6 sample shows negligible emission peak when excited, which is centered at 454 nm. The PL and PLE spectra of pristine Cs_2SnCl_6 are showed in Fig. S1.†Fortunately, for the Cs_2SnCl_6:$Bi_{0.2}$ sample, there is a strong peak centered at 454 nm. What's more, as the

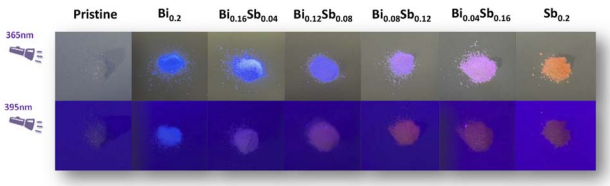

Fig. 2 Photograph of pristine Cs_2SnCl_6 and Cs_2SnCl_6:$Bi_{0.2-x}Sb_x$ (x = 0.04, 0.08, 0.12, 0.16, 0.2) crystals irradiated by a UV lamp at 365 nm and 395 nm.

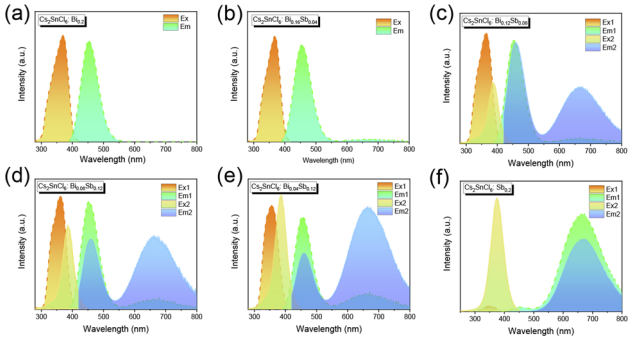

Fig. 3 (a–f) PLE and PL spectrum of Cs_2SnCl_6:$Bi_{0.2-x}Sb_x$ (x = 0, 0.04, 0.08, 0.12, 0.16, 0.2). Note: Ex1 = 365 nm, Ex2 = 395 nm.

Sb^{3+} content increased in Cs_2SnCl_6:$Bi_{0.2-x}Sb_x$, the intensity of peak centered at 666 nm enhanced and peak centered at 454 nm attenuated gradually. When the Sb^{3+} reached the maximum ratio of Cs_2SnCl_6:$Sb_{0.2}$, the peak of 454 nm reached to the minina. In the meanwhile, the emission peak of 666 nm reached the maximum intensity. The PL spectrum of different co-doping Bi^{3+}/Sb^{3+} content of Cs_2SnCl_6 exhibited similar trend but different PL intensity when excited by the excitation light of 395 nm. The Commission Internationale de l'Eclairage (CIE) coordinate at (0.1419, 0.0728), (0.1503, 0.0847), (0.1586, 0.0895), (0.1717, 0.0966), (0.1939, 0.1139), (0.5757, 0.3792) when excited at 365 nm and (0.1416, 0.0729), (0.1580, 0.0843), (0.2758, 0.1798), (0.3434, 0.2200), (0.4107, 0.2613), (0.6093, 0.3848) when excited at 395 nm for Cs_2SnCl_6:$Bi_{0.2-x}Sb_x$ (x = 0, 0.04, 0.08, 0.12, 0.16, 0.2), which are marked in the CIE chromaticity diagram (Fig. S2†). The marked points in Fig. S2b† are relatively evenly distributed compared to Fig. S2a,† which is consistent with the PL phenomenon. Inspired by the interesting PL phenomenon, Cs_2SnCl_6:$Bi_{0.08}Sb_{0.12}$, which has the distinct difference of PL phenomenon (Fig. 2), was characterized by variable excitation wavelength PL spectrum.

Fig. 4a shows the different patterns composed by Cs_2SnCl_6:$Bi_{0.08}Sb_{0.12}$ powder at natural light and irradiated by a UV lamp at 365 nm and 395 nm. When the Cs_2SnCl_6:$Bi_{0.08}Sb_{0.12}$ crystals are ground into a powder, it can be processed into any shape. The pattern shows blue and bright red patterns when irradiated by 365 and 395 nm UV light, respectively. What's more, Fig. S3† shows the school emblem printed by the anti-counterfeiting ink, which is composed of Cs_2SnCl_6:$Bi_{0.08}Sb_{0.12}$ powder, dispersant and solvents. The photos were taken in natural light and irradiated by a UV lamp at 365 nm and 395 nm. The pattern shows blue and bright red patterns when irradiated by 365 and 395 nm UV light, respectively. This demonstrated the Cs_2SnCl_6:$Bi_{0.08}Sb_{0.12}$ crystals are excellent anti-counterfeiting material, which can be applied into anti-counterfeiting technology. In Fig. 4b, there is an excitation-wavelength-dependent dual-emission phenomenon for the Cs_2SnCl_6:$Bi_{0.08}Sb_{0.12}$ sample when the excitation wavelength varied from 320 to 420 nm. From 320 to 350 nm, there is only one peak centered at 454 nm, the intensity of which enhanced gradually as the excitation wavelength increased. At the same time, the peak centered at 666 nm appeared when the excitation wavelength increased to 350 nm. When the Ex = 360 nm, the intensity of the emission peak at 454 nm reached its maximum. With the excitation wavelength increasing from 360 to 390 nm, the intensity of peak at 454 nm attenuated and the peak at 666 nm enhanced inch by inch. When the excitation wavelength varied between 400 to 420 nm, both of the two peaks attenuated simultaneously. The CIE chromaticity coordinates of Cs_2SnCl_6:$Bi_{0.08}Sb_{0.12}$ at different excited wavelength from 320 nm to 420 nm showed the obvious excitation-dependent photoluminescence phenomenon (Fig. 4c). The photoluminescence of the co-doped material covers a wide color gamut, which is hard to be copied. The optical material is not easy to replicate because of its unique photoluminescence properties. This intriguing optical property enable us to apply this material into optical anti-counterfeiting applications.

Excellent PL and chemical stability is fundamental to optical anti-counterfeiting materials. Herein, the thermogravimetric analysis (TGA) was applied for pristine Cs_2SnCl_6 and Cs_2SnCl_6:$Bi_{0.2-x}Sb_x$ (x = 0, 0.04, 0.08, 0.12, 0.16, 0.2). From the

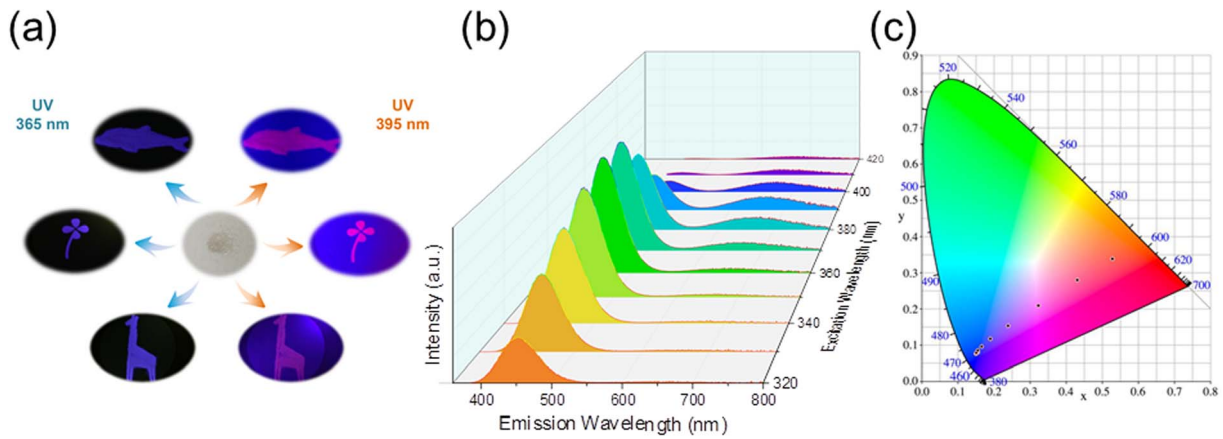

Fig. 4 (a) Photograph of Cs_2SnCl_6:$Bi_{0.08}Sb_{0.12}$ at natural light and irradiated by a UV lamp at 365 nm and 395 nm. (b) PL spectrum of variable excitation wavelength for Cs_2SnCl_6:$Bi_{0.08}Sb_{0.12}$ sample. (c) The CIE chromaticity coordinates of Cs_2SnCl_6:$Bi_{0.08}Sb_{0.12}$ at different excited wavelength from 320 nm to 420 nm.

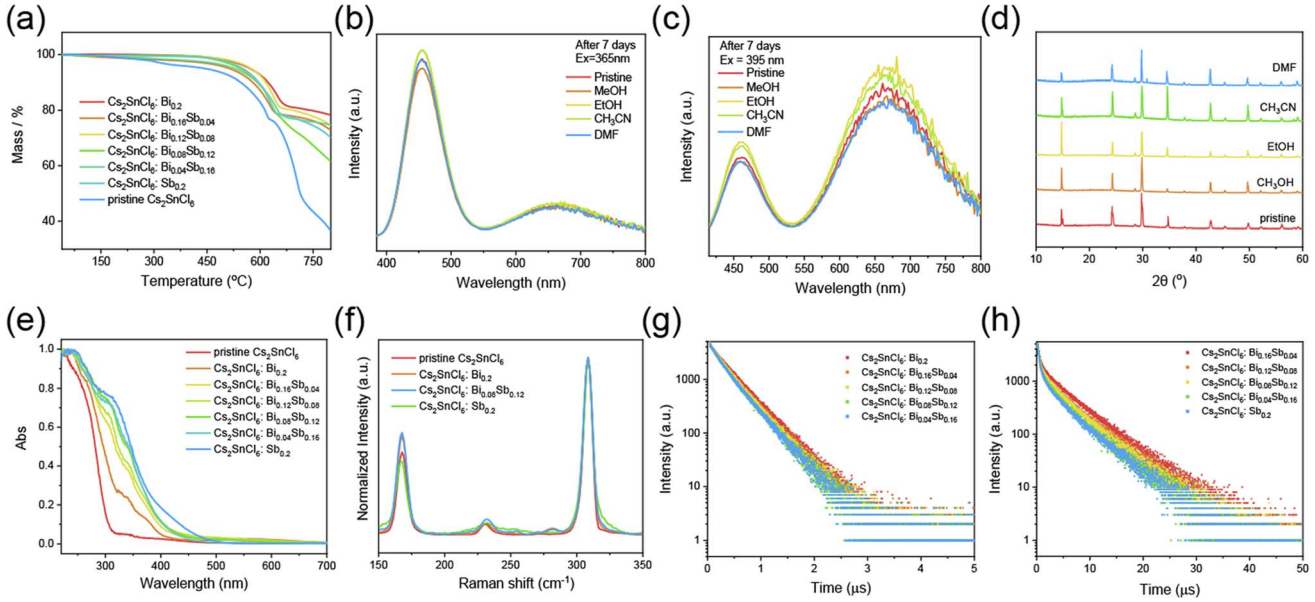

Fig. 5 (a) The TGA curves of pristine Cs_2SnCl_6 and Cs_2SnCl_6:$Bi_{0.2-x}Sb_x$ (x = 0, 0.04, 0.08, 0.12, 0.16, 0.2) metal halides crystals. PL spectrum excited by 365 nm (b) and 395 nm (c) of pristine Cs_2SnCl_6:$Bi_{0.08}Sb_{0.12}$ and Cs_2SnCl_6:$Bi_{0.08}Sb_{0.12}$ after being soked in different solvent for a week. (d) PXRD pattern of pristine Cs_2SnCl_6:$Bi_{0.08}Sb_{0.12}$ and Cs_2SnCl_6:$Bi_{0.08}Sb_{0.12}$ after being soked in different solvent for a week. (e) UV-visible absorption spectrum (f) Raman spectrum of Cs_2SnCl_6, Cs_2SnCl_6:$Bi_{0.2}$, Cs_2SnCl_6:$Bi_{0.08}Sb_{0.12}$ and Cs_2SnCl_6:$Sb_{0.2}$ sample. (g) TRPL spectra of Cs_2SnCl_6:$Bi_{0.2-x}Sb_x$ sample at 454 nm (x = 0, 0.04, 0.08, 0.12, 0.16). (h) TRPL spectra of Cs_2SnCl_6:$Bi_{0.2-x}Sb_x$ sample at 666 nm (x = 0.04, 0.08, 0.12, 0.16, 0.2).

Fig. 5a we can find that the pristine Cs_2SnCl_6 crystals would dehydrate in the beginning. Then, it became to decompose at 300 °C. With the temperature going on constantly, the crystals began to decompose into $SnCl_4$ (Fig. S4†).[44] Encouragingly, there is no obvious decomposition observed until 450 °C in the thermogravimetric analysis (TGA) of the Cs_2SnCl_6:$Bi_{0.2-x}Sb_x$ crystals, which indicated the dopants enhanced the thermal stability of the pristine Cs_2SnCl_6 crystals. When the Cs_2SnCl_6:-$Bi_{0.08}Sb_{0.12}$ crystals were soaked in DMF, DMSO, CH_3OH, CH_3-CH_2OH and CH_3CN for a week, there is no distinct difference between the crystals soaked in different solvent and the pristine one in PL intensity (Fig. 5b and c). In addition, the PXRD for crystals soaked in different solvents shows similar pattern, which demonstrate the high chemical stability for the crystals (Fig. 5d). The excellent thermal and PL stability demonstrate it has great potential to be applied into the optical anti-counterfeiting application.

To further reveal the reasons for the differences in crystal properties after doping, we also did some other characterization. The UV-vis spectrum curves are shown in Fig. 5e. New absorption peaks appear at 340 nm and 313 nm in Cs_2SnCl_6:-$Bi_{0.2}$ and Cs_2SnCl_6:$Sb_{0.2}$, which can be ascribed to the impurity doping of Bi^{3+} and Sb^{3+}, respectively.

For the fact that Raman spectroscopy can directly reveal the phonon coupling to the electronic transition between the excited and ground states, it was further employed to shed light on the exciton–phonon interactions.[45] The laser of 532 nm was used as the excitation light to eliminate the interference from PL. In Fig. 5f, four samples (the pristine Cs_2SnCl_6, Cs_2SnCl_6:-$Bi_{0.2}$, Cs_2SnCl_6:$Bi_{0.08}Sb_{0.12}$ and Cs_2SnCl_6:$Sb_{0.2}$) were tested. All of them exhibit three intense bands at 168, 232 and 309 cm^{-1} that are assigned to symmetric stretching (A_{1g}), asymmetric stretching (E_g) and $2A_{1g}$ vibrational modes in metal halide octahedron.[46–48] When Bi^{3+} was doped, the peak at 280 cm^{-1} which ascribed to the A_{1g} stretching appeared.[49] And the peak at 254 cm^{-1} ascribed to A_{1g} stretching as well appeared once Sb^{3+} was doped.[49] As the content of Sb^{3+} increased, the intensity of peaks at 168 and 232 cm^{-1} decreased, indicating that the vibrational modes of metal halide octahedron have substantially weaker coupling strength. The vibrational overlap between the excited and ground-state vibrational wavefunctions was further decreased. As a result, the nonradiative processes were suppressed, which may account for the higher PLQY for Cs_2-$SnCl_6$:$Bi_{0.2}$ than Cs_2SnCl_6:$Sb_{0.2}$.[50]

The Fig. 5g and h show the TRPL spectra of Cs_2SnCl_6:-$Bi_{0.2-x}Sb_x$ (x = 0, 0.04, 0.08, 0.12, 0.16) at 454 nm and Cs_2-$SnCl_6$:$Bi_{0.2-x}Sb_x$ (x = 0.04, 0.08, 0.12, 0.16, 0.2) at 666 nm, respectively. The peak centered at 454 nm has monoexponential PL decay while the peak centered at 666 nm has double-exponential decay.[51] The data of lifetime for these two peaks at different content of impurity doping are given in Table S2.† From the Fig. 5g, h and Table S2,† we find that both of the lifetime of radiation recombination for peaks at 454 nm and the peak at 666 nm increased with more component content of Bi^{3+} and less component of Sb^{3+}. The highest PLQY above these crystals is Cs_2SnCl_6:$Bi_{0.2}$, which is up to 40.91%. And the PLQY of Cs_2SnCl_6:$Sb_{0.2}$ is 8.76%.

In Fig. 6a and b, the temperature-dependent PL spectrum of Cs_2SnCl_6:$Bi_{0.2}$ and Cs_2SnCl_6:$Sb_{0.2}$ displays that the PL intensities increase as the temperature drops from 280 K to 140 K,

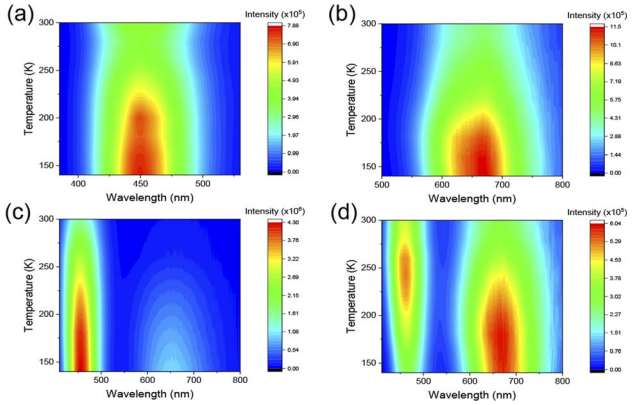

Fig. 6 Temperature-dependent PL spectrum of Cs_2SnCl_6:$Bi_{0.2}$ (a) Cs_2SnCl_6:$Sb_{0.2}$ (b), Cs_2SnCl_6:$Bi_{0.08}Sb_{0.12}$ at 365 nm (c) and 395 nm (d).

while the signal of emission peak for both two materials is continuously enhanced. This phenomenon reflects the non-radiative recombination process is suppressed in the low temperature region.[52] The temperature-dependent integrated PL intensity was shown in Fig. S5.† The exciton binding energy (E_b) can be calculated by the following Arrhenius eqn (1).

$$I(T) = \frac{I_0}{1 + A\exp\left(\frac{-E_b}{K_B T}\right)} \quad (1)$$

where k_B is Boltzmann constant, T temperature, I_0 PL integrated intensity at 0 K, I PL integrated intensity.[53] Conductive to radiative recombination, the E_b value of Cs_2SnCl_6:$Bi_{0.2}$ and Cs_2SnCl_6:$Sb_{0.2}$ is calculated as 133 and 104 meV, respectively through the fitting curves of integrated PL intensity and temperature, which is much higher than the traditional 3D perovskites such as $MAPbI_3$ and $CsSnI_3$. The high value of E_b shows excitons in Cs_2SnCl_6:$Bi_{0.2}$ and Cs_2SnCl_6:$Sb_{0.2}$ are typical Frenkel excitons.[54] The resulting highly localized excitons with stronger binding reduce the probability for carrier scattering, which further suppressed the non-radiative recombination significantly.[55]

According to the previous report, the photoluminescence of Cs_2SnCl_6:$Bi_{0.2}$ can be ascribed to the [Bi_{Sn} + V_{Cl}] defect complex.[56] The photoluminescence of Cs_2SnCl_6:$Sb_{0.2}$ is originted from triplet self-trapped excitons, attributed to the ^3P_n–$^1S_0$ transitions (n = 0, 1, 2).[34] Therefore, we propose the energy transfer (ET) process between dopants as shown in Fig. S6.† Besides, from the Table S2,† we can find that the lifetime of Cs_2SnCl_6:$Bi_{0.2-x}Sb_x$ (x = 0.04, 0.08, 0.12, 0.16, 0.2) at 666 nm becomes longer as the content of Bi^{3+} increases (Fig. S7†). Combined with the temperature-dependent photoluminescence phenomenon in Fig. 6d where the intensity of peak at 454 nm enhanced and then attenuated from 300 K to 140 K, it is speculated that there is an energy transfer process between [Bi_{Sn} + V_{Cl}] and STEs formed by Sb^{3+}.

In order to further confirm the existence of Bi^{3+} and Sb^{3+} ions, XPS were also applied. The full range XPS spectrum for the two samples mentioned above was showed in Fig. S8a.† The Fig. S8b–f† showed the high-resolution XPS spectrum of Cs 3d, Sn 3d, Cl 2p and Sb 3d for pristine Cs_2SnCl_6 and Cs_2SnCl_6:$Bi_{0.08}Sb_{0.12}$ sample. As shown in Fig. S8c,† the Sn 3d spectra of pristine Cs_2SnCl_6 sample has two signature peaks of Sn $3d_{3/2}$ and Sn $3d_{5/2}$ at 495.6 and 487.1 eV.[57] In addition, the Cl 2p spectrum of the pristine Cs_2SnCl_6 sample showed main peaks of Cl $2p_{1/2}$ and Cl $2p_{3/2}$ at 199.9 and 198.3 eV (Fig. S8d†).[58] The Cs 3d spectrum showed two main peak of Cs $3d_{3/2}$ and Cs $3d_{5/2}$ at 738.7 and 724.6 eV (Fig. S8b†). However, when the Bi^{3+} and Sb^{3+} were induced to the Cs_2SnCl_6 crystals, the Bi 4f spectrum showed two main peaks of Bi $4f_{5/2}$ and $4f_{7/2}$ at 164.2 eV and 159.2 eV, and the Sb 3d spectrum showed two main peaks of Sb $3d_{3/2}$ and Sb $3d_{5/2}$ at 539.5 and 531.9 eV, respectively.[34] A slight O 1s signal is inevitably detected due to oxygen and moisture in the air.[59] What's more, the binding energy of Sn^{4+} $3d_{3/2}$ and Sn^{4+} $3d_{5/2}$, Cl $2p_{1/2}$ and Cl $2p_{3/2}$ move to lower energy while the binding energy of Cs $3d_{3/2}$ and Cs $3d_{5/2}$ remain unchanged. These results indicate that some Bi^{3+} and Sb^{3+} ions have entered into the lattice of the Cs_2SnCl_6 host and most probably substituted on the Sn^{4+} sites. Moreover, with the addition of Bi^{3+} and Sb^{3+} ions, there is a partial decreasement in the interaction between extranuclear and core electrons in both neighboring Sn^{4+} and Cl^-, accounting for the peak shift to lower energy in Cs_2SnCl_6:$Bi_{0.08}Sb_{0.12}$ sample.[60]

Experimental

Materials

Cesium chloride (AR), stannous(II) mono-sulphate (AR), bismuth(III) chloride (AR) and antimony(III) chloride purchased from Sigma Aldrich. Hydrochloric acid was purchased from Sinopharm Chemical Reagent Co., Ltd. All reagents and solvents were used without further purification.

Synthesis

Cs_2SnCl_6. A mixture of cesium chloride (0.063 g, 0.375 mmol) and stannous mono-sulphate (0.020 g, 0.094 mmol) were first dissolved in Teflon autoclave with 10 mL hydrochloric acid. Then the solution was heated at 90 °C for 1 h in a stainless steel Parr autoclave. The solution was then slowly cooled to 30 °C with a speed of 2 °C h^{-1}. The as-synthesized crystals were then filtered out and washed with isopropanol and dried in a furnace overnight at 30 °C.

Cs_2SnCl_6:$Bi_xSb_{0.2-x}$. A mixture of cesium chloride (0.063 g, 0.375 mmol), stannous mono-sulphate (0.020 g, 0.094 mmol) and 0.0188 mmol impurity of bismuth chloride and antimony chloride were first dissolved in Teflon autoclave with 10 mL hydrochloric acid. Then the solution was heated at 90 °C for 1 h in a stainless steel Parr autoclave. The solution was then slowly cooled to 30 °C with a speed of 2 °C h^{-1}. The as-synthesized crystals were then filtered out and washed with isopropanol and dried in a furnace overnight at 30 °C.

Cs_2SnCl_6:$Bi_{0.08}Sb_{0.12}$. A mixture of cesium chloride (0.063 g, 0.375 mmol), stannous mono-sulphate (0.020 g, 0.094 mmol), bismuth chloride (0.0024 g, 0.00752 mmol) and antimony chloride (0.0026 g, 0.01128 mmol) were first dissolved in Teflon autoclave with 10 mL hydrochloric acid. Then the solution was

heated at 90 °C for 1 h in a stainless steel Parr autoclave. The solution was then slowly cooled to 30 °C with a speed of 2 °C h^{-1}. The as-synthesized crystals were then filtered out and washed with isopropanol and dried in a furnace overnight at 30 °C.

Anti-counterfeiting ink. The ethylene glycol, diethylene glycol monomethyl ether, and propylene glycol methyl ether were mixed in a weight ratio of 3 : 5 : 2 as the ink solvent. Then, the Cs_2SnCl_6:$Bi_{0.08}Sb_{0.12}$ was put into the ink solvent, and 1 wt% of dispersant BYK110 was added according to the weight of the powder. Put the mixture of ink solvent, powder and dispersant in a ball mill tank, and use a planetary ball mill to mix and disperse at a speed of 400 rpm for 5 h. The prepared mixture is filtered through a 1 micron filter membrane to prepare an inkjet printable ink.

The piezoelectric inkjet printing process (BroadTeko DP800 inkjet Printer) was used. The school emblem and the square array were successfully printed at a resolution of 1200 × 1200.

Characterization

Powder X-ray diffraction (PXRD) patterns were tested on a Rigaku D/max-IIIA diffractometer with Cu Kα (1.54 Å) radiation at 293 K. Steady-state PL spectrums were recorded by Edinburgh Instruments FLS 980 at room temperature (25 °C) for all samples. Diffuse reflectance spectrums of the microcrystalline powders were recorded on a UV/Vis spectrophotometer (SHIMADZU, UV3600Plus), calibrated by simultaneous measurement of the substance ($BaSO_4$ powder), and then converted to absorbance using the KubelkaMunk theory. The thickness and roughness of the samples remained consistent during the study with different doping levels. Thermogravimetric Analysis spectrums were measured on NETZSCH TG209F3 with the heating rate of 10 K per minute in N_2 atmosphere. Raman spectrums were obtained on RENISHAW inVia Reflex. The XPS measurements were performed on Thermal Scientific Escalab 250 Xi-UPS. An Al Kα (1486.6 eV) X-ray was used as the excitation source for XPS.

Conclusions

In this work, Bi^{3+} and Sb^{3+} co-doped zero-dimensional Cs_2SnCl_6 metal halide material is synthesized by co-doping method, which exhibit tunable emission covering a wide region of color. The impurities improve the pristine Cs_2SnCl_6 in stability against air, high temperature and organic solvents. By adjusting the relative co-doping content of two ions, we can target the desired PL phenomenon. The PL emission peak centered at 454 and 666 nm in Bi^{3+} and Sb^{3+} co-doped Cs_2SnCl_6 can be ascribed to the $[Bi_{Sn} + V_{Cl}]$ defect and STEs. The Cs_2SnCl_6:$Bi_{0.08}Sb_{0.12}$ with excitation-wavelength-dependent emission phenomenon is highly stable and environmental-friendly, which can highly meet our practical demands. This single component and tunable luminescent material with high stability is promising to be applied into optical anti-counterfeiting technology. Additionally, co-doping method can provide a new way for researchers to enrich the luminescence of metal halide perovskite.

Conflicts of interest

There are no conflicts to declare.

Acknowledgements

This work is supported by National Natural Science Foundation of China (Grant No. 22005089), Natural Science Foundation of Hubei Province (Grant No. 2020CFB146), Hubei Provincial Department of Education (Grant No. Q20201002), Hubei University, Wuhan, 430062, P. R. China, National College Students' Innovation and Entrepreneurship Training Programs (Grant No. 202210512007).

Notes and references

1 E. L. Prime and D. H. Solomon, Australia's Plastic Banknotes: Fighting Counterfeit Currency, *Angew. Chem., Int. Ed.*, 2010, **49**, 3726–3736.
2 K. Jiang, L. Zhang, J. Lu, C. Xu, C. Cai and H. Lin, Triple-Mode Emission of Carbon Dots: Applications for Advanced Anti-Counterfeiting, *Angew. Chem., Int. Ed.*, 2016, **55**, 7231–7235.
3 Z. Gao, Y. Han and F. Wang, Cooperative supramolecular polymers with anthracene–endoperoxide photo-switching for fluorescent anti-counterfeiting, *Nat. Commun.*, 2018, **9**, 3977.
4 Z. Sun, J. Yang, L. Huai, W. Wang, Z. Ma, J. Sang, J. Zhang, H. Li, Z. Ci and Y. Wang, Spy Must Be Spotted: A Multistimuli-Responsive Luminescent Material for Dynamic Multimodal Anticounterfeiting and Encryption, *ACS Appl. Mater. Interfaces*, 2018, **10**, 21451–21457.
5 W. Ren, G. Lin, C. Clarke, J. Zhou and D. Jin, Optical Nanomaterials and Enabling Technologies for High-Security-Level Anticounterfeiting, *Adv. Mater.*, 2020, **32**, 1901430.
6 L. Xu, J. Chen, J. Song, J. Li, J. Xue, Y. Dong, B. Cai, Q. Shan, B. Han and H. Zeng, Double-Protected All-Inorganic Perovskite Nanocrystals by Crystalline Matrix and Silica for Triple-Modal Anti-Counterfeiting Codes, *ACS Appl. Mater. Interfaces*, 2017, **9**, 26556–26564.
7 J. Deng, L. Deng, Z. Guan, J. Tao, G. Li, Z. Li, Z. Li, S. Yu and G. Zheng, Multiplexed Anticounterfeiting Meta-image Displays with Single-Sized Nanostructures, *Nano Lett.*, 2020, **20**, 1830–1838.
8 S. Han, H. J. Bae, J. Kim, S. Shin, S.-E. Choi, S. H. Lee, S. Kwon and W. Park, Lithographically Encoded Polymer Microtaggant Using High-Capacity and Error-Correctable QR Code for Anti-Counterfeiting of Drugs, *Adv. Mater.*, 2012, **24**, 5924–5929.
9 J. Sang, J. Zhou, J. Zhang, H. Zhou, H. Li, Z. Ci, S. Peng and Z. Wang, Multilevel Static–Dynamic Anticounterfeiting Based on Stimuli-Responsive Luminescence in a Niobate Structure, *ACS Appl. Mater. Interfaces*, 2019, **11**, 20150–20156.

10 Y. Hu, Q. Shao, X. Deng, D. Song, S. Han, Y. Dong and J. Jiang, Thermally induced multicolor emissions of upconversion hybrids with large color shifts for anticounterfeiting applications, *J. Mater. Chem. C*, 2019, **7**, 11770–11775.

11 M. Ataeefard and F. Nourmohammadian, Producing fluorescent digital printing ink: Investigating the effect of type and amount of coumarin derivative dyes on the quality of ink, *J. Lumin.*, 2015, **167**, 254–260.

12 X. Li, S. Xu, F. Liu, J. Qu, H. Shao, Z. Wang, Y. Cui, D. Ban and C. Wang, Bi and Sb Codoped Cs2Ag0.1Na0.9InCl6 Double Perovskite with Excitation-Wavelength-Dependent Dual-Emission for Anti-Counterfeiting Application, *ACS Appl. Mater. Interfaces*, 2021, **13**, 31031–31037.

13 L. N. Quan, B. P. Rand, R. H. Friend, S. G. Mhaisalkar, T.-W. Lee and E. H. Sargent, Perovskites for Next-Generation Optical Sources, *Chem. Rev.*, 2019, **119**, 7444–7477.

14 J. Luo, X. Wang, S. Li, J. Liu, Y. Guo, G. Niu, L. Yao, Y. Fu, L. Gao, Q. Dong, C. Zhao, M. Leng, F. Ma, W. Liang, L. Wang, S. Jin, J. Han, L. Zhang, J. Etheridge, J. Wang, Y. Yan, E. H. Sargent and J. Tang, Efficient and stable emission of warm-white light from lead-free halide double perovskites, *Nature*, 2018, **563**, 541–545.

15 Y. J. Yoon, K. T. Lee, T. K. Lee, S. H. Kim, Y. S. Shin, B. Walker, S. Y. Park, J. Heo, J. Lee, S. K. Kwak, G.-H. Kim and J. Y. Kim, Reversible, Full-Color Luminescence by Post-treatment of Perovskite Nanocrystals, *Joule*, 2018, **2**, 2105–2116.

16 M. Lyu, J.-H. Yun, P. Chen, M. Hao and L. Wang, Addressing Toxicity of Lead: Progress and Applications of Low-Toxic Metal Halide Perovskites and Their Derivatives, *Adv. Energy Mater.*, 2017, **7**, 1602512.

17 M. L. Davies, Addressing the Stability of Lead Halide Perovskites, *Joule*, 2020, **4**, 1626–1627.

18 S. Jia, G. Li, P. Liu, R. Cai, H. Tang, B. Xu, Z. Wang, Z. Wu, K. Wang and X. W. Sun, Highly Luminescent and Stable Green Quasi-2D Perovskite-Embedded Polymer Sheets by Inkjet Printing, *Adv. Funct. Mater.*, 2020, **30**, 1910817.

19 H.-P. Wang, S. Li, X. Liu, Z. Shi, X. Fang and J.-H. He, Low-Dimensional Metal Halide Perovskite Photodetectors, *Adv. Mater.*, 2021, **33**, 2003309.

20 C. Zhou, Y. Tian, M. Wang, A. Rose, T. Besara, N. K. Doyle, Z. Yuan, J. C. Wang, R. Clark, Y. Hu, T. Siegrist, S. Lin and B. Ma, Low-Dimensional Organic Tin Bromide Perovskites and Their Photoinduced Structural Transformation, *Angew. Chem., Int. Ed.*, 2017, **56**, 9018–9022.

21 Y. Zhang, X. Liu, H. Sun, J. Zhang, X. Gao, C. Yang, Q. Li, H. Jiang, J. Wang and D. Xu, Strong Self-Trapped Exciton Emissions in Two-Dimensional Na-In Halide Perovskites Triggered by Antimony Doping, *Angew. Chem., Int. Ed.*, 2021, **60**, 7587–7592.

22 S. Li, J. Luo, J. Liu and J. Tang, Self-Trapped Excitons in All-Inorganic Halide Perovskites: Fundamentals, Status, and Potential Applications, *J. Phys. Chem. Lett.*, 2019, **10**, 1999–2007.

23 P. Han, C. Luo, S. Yang, Y. Yang, W. Deng and K. Han, All-Inorganic Lead-Free 0D Perovskites by a Doping Strategy to Achieve a PLQY Boost from <2% to 90%, *Angew. Chem., Int. Ed.*, 2020, **59**, 12709–12713.

24 L. Zhou, J.-F. Liao, Z.-G. Huang, J.-H. Wei, X.-D. Wang, W.-G. Li, H.-Y. Chen, D.-B. Kuang and C.-Y. Su, A Highly Red-Emissive Lead-Free Indium-Based Perovskite Single Crystal for Sensitive Water Detection, *Angew. Chem., Int. Ed.*, 2019, **58**, 5277–5281.

25 C. Yang, F. Guo, Y. Zhang, X. Zhong, J. Feng, N. Wang and J. Wang, Luminescence Change from Orange to Blue for Zero-Dimensional Cs2InCl5(H2O) Metal Halides in Water and a New Post-doping Method, *Chem.–Asian J.*, 2021, **16**, 1619–1625.

26 A. Veronese, M. Patrini, D. Bajoni, C. Ciarrocchi, P. Quadrelli and L. Malavasi, Highly Tunable Emission by Halide Engineering in Lead-Free Perovskite-Derivative Nanocrystals: The Cs2SnX6 (X = Cl, Br, Br/I, I) System, *Front. Chem.*, 2020, **8**, 35.

27 A. Wang, X. Yan, M. Zhang, S. Sun, M. Yang, W. Shen, X. Pan, P. Wang and Z. Deng, Controlled Synthesis of Lead-Free and Stable Perovskite Derivative Cs2SnI6 Nanocrystals via a Facile Hot-Injection Process, *Chem. Mater.*, 2016, **28**, 8132–8140.

28 S.-C. Lim, H.-P. Lin, W.-L. Tsai, H.-W. Lin, Y.-T. Hsu and H.-Y. Tuan, Binary halide, ternary perovskite-like, and perovskite-derivative nanostructures: hot injection synthesis and optical and photocatalytic properties, *Nanoscale*, 2017, **9**, 3747–3751.

29 A. Karmakar, S. Mukhopadhyay, P. G. B. Gachod, V. A. Mora-Gomez, G. M. Bernard, A. Brown and V. K. Michaelis, Uncovering Halogen Mixing and Octahedral Dynamics in Cs2SnX6 by Multinuclear Magnetic Resonance Spectroscopy, *Chem. Mater.*, 2021, **33**, 6078–6090.

30 Z. Pan, B. Liu, B. Wang, Y. Liu, T. Si, W. Yi, Y. Wu, J. Li and B. Cao, Lead-free Cs2SnX6 (X = Cl, Br, I) nanocrystals in mesoporous SiO2 with more stable emission from VIS to NIR light, *Chem. Phys. Lett.*, 2021, **782**, 139023.

31 M. M. S. Karim, A. M. Ganose, L. Pieters, W. W. Winnie Leung, J. Wade, L. Zhang, D. O. Scanlon and R. G. Palgrave, Anion Distribution, Structural Distortion, and Symmetry-Driven Optical Band Gap Bowing in Mixed Halide Cs2SnX6 Vacancy Ordered Double Perovskites, *Chem. Mater.*, 2019, **31**, 9430–9444.

32 J. Zhou, J. Luo, X. Rong, P. Wei, M. S. Molokeev, Y. Huang, J. Zhao, Q. Liu, X. Zhang, J. Tang and Z. Xia, Lead-Free Perovskite Derivative Cs2SnCl6−xBrx Single Crystals for Narrowband Photodetectors, *Adv. Opt. Mater.*, 2019, **7**, 1900139.

33 Z. Tan, J. Li, C. Zhang, Z. Li, Q. Hu, Z. Xiao, T. Kamiya, H. Hosono, G. Niu, E. Lifshitz, Y. Cheng and J. Tang, Highly Efficient Blue-Emitting Bi-Doped Cs2SnCl6 Perovskite Variant: Photoluminescence Induced by Impurity Doping, *Adv. Funct. Mater.*, 2018, **28**, 1801131.

34 Y. Jing, Y. Liu, J. Zhao and Z. Xia, Sb3+ Doping-Induced Triplet Self-Trapped Excitons Emission in Lead-Free

Cs2SnCl6 Nanocrystals, *J. Phys. Chem. Lett.*, 2019, **10**, 7439–7444.

35 A. Yan, K. Li, Y. Zhou, Y. Ye, X. Zhao and C. Liu, Tuning the optical properties of Cs2SnCl6:Bi and Cs2SnCl6:Sb lead-free perovskites via post-annealing for white LEDs, *J. Alloys Compd.*, 2020, **822**, 153528.

36 Y. Zhong, Y.-E. Huang, T. Deng, Y.-T. Lin, X.-Y. Huang, Z.-H. Deng and K.-Z. Du, Multi-Dopant Engineering in Perovskite Cs_2SnCl_6: White Light Emitter and Spatially Luminescent Heterostructure, *Inorg. Chem.*, 2021, **60**, 17357–17363.

37 X. Liu, X. Xu, B. Li, L. Yang, Q. Li, H. Jiang and D. Xu, Tunable Dual-Emission in Monodispersed Sb3+/Mn2+ Codoped Cs2NaInCl6 Perovskite Nanocrystals through an Energy Transfer Process, *Small*, 2020, **16**, 2002547.

38 W. Zhang, W. Zheng, L. Li, P. Huang, Z. Gong, Z. Zhou, J. Sun, Y. Yu and X. Chen, Dual-Band-Tunable White-Light Emission from Bi3+/Te4+ Emitters in Perovskite-Derivative Cs2SnCl6 Microcrystals, *Angew. Chem., Int. Ed.*, 2022, **61**, e202116085.

39 S. Gong, R. Wu, S. Yang, L. Wu, M. Zhang, Q. Han and W. Wu, Tuning the luminous properties and optical thermometry of Cs2SnCl6 phosphor microcrystals via Bi and Sb codoping, *Photon. Res.*, 2021, **9**, 2182–2189.

40 Y. Liu, X. Rong, M. Li, M. S. Molokeev, J. Zhao and Z. Xia, Incorporating Rare-Earth Terbium(III) Ions into Cs2AgInCl6:Bi Nanocrystals toward Tunable Photoluminescence, *Angew. Chem., Int. Ed.*, 2020, **59**, 11634–11640.

41 Y. Zhou, Z.-J. Yong, K.-C. Zhang, B.-M. Liu, Z.-W. Wang, J.-S. Hou, Y.-Z. Fang, Y. Zhou, H.-T. Sun and B. Song, Ultrabroad Photoluminescence and Electroluminescence at New Wavelengths from Doped Organometal Halide Perovskites, *J. Phys. Chem. Lett.*, 2016, **7**, 2735–2741.

42 H. Miao, C. Ding and H. Luo, Antimony-doped tin dioxide nanometer powders prepared by the hydrothermal method, *Microelectron. Eng.*, 2003, **66**, 142–146.

43 R. Zhang, X. Mao, Y. Yang, S. Yang, W. Zhao, T. Wumaier, D. Wei, W. Deng and K. Han, Air-Stable, Lead-Free Zero-Dimensional Mixed Bismuth-Antimony Perovskite Single Crystals with Ultra-broadband Emission, *Angew. Chem., Int. Ed.*, 2019, **58**, 2725–2729.

44 Q. Ba, J. Kim, H. Im, S. Lin and A. Jana, Modulation of the optical bandgap and photoluminescence quantum yield in pnictogen (Sb3+/Bi3+)-doped organic–inorganic tin(IV) perovskite single crystals and nanocrystals, *J. Colloid Interface Sci.*, 2022, **606**, 808–816.

45 S. Reichardt and L. Wirtz, Nonadiabatic exciton-phonon coupling in Raman spectroscopy of layered materials, *Sci. Adv.*, 2020, **6**, eabb5915.

46 S. BelhajSalah, M. S. M. Abdelbaky, S. García-Granda, K. Essalah, C. Ben Nasr and M. L. Mrad, Synthesis, crystal structure, vibrational, optical properties, thermal analysis and theoretical study of a new Sn(IV) complex (C5H14N2)2 [SnCl6]2·5H2O, *Solid State Sci.*, 2018, **86**, 77–85.

47 B. Zhou, Z. Liu, S. Fang, H. Zhong, B. Tian, Y. Wang, H. Li, H. Hu and Y. Shi, Efficient White Photoluminescence from Self-Trapped Excitons in Sb3+/Bi3+-Codoped Cs2NaInCl6 Double Perovskites with Tunable Dual-Emission, *ACS Energy Lett.*, 2021, **6**, 3343–3351.

48 Z. Tan, Y. Chu, J. Chen, J. Li, G. Ji, G. Niu, L. Gao, Z. Xiao and J. Tang, Lead-Free Perovskite Variant Solid Solutions Cs2Sn1–xTexCl6: Bright Luminescence and High Anti-Water Stability, *Adv. Mater.*, 2020, **32**, 2002443.

49 W. Smit, G. J. Dirksen, D. J. J. J. o. P. Stufkens and C. o. Solids, Infrared and Raman spectra of the elpasolites Cs2NaSbCl6 and Cs2NaBiCl6: Evidence for a pseudo Jahn-Teller distorted ground state, *J. Phys. Chem. Solids*, 1990, **51**, 189–196.

50 L. Zhou, J.-F. Liao, Y. Qin, X.-D. Wang, J.-H. Wei, M. Li, D.-B. Kuang and R. He, Activation of Self-Trapped Emission in Stable Bismuth-Halide Perovskite by Suppressing Strong Exciton–Phonon Coupling, *Adv. Funct. Mater.*, 2021, **31**, 2102654.

51 Y. Sun, A. J. Fernández-Carrión, Y. Liu, C. Yin, X. Ming, B.-M. Liu, J. Wang, H. Fu, X. Kuang and X. Xing, Bismuth-Based Halide Double Perovskite Cs2LiBiCl6: Crystal Structure, Luminescence, and Stability, *Chem. Mater.*, 2021, **33**, 5905–5916.

52 L. Zhou, J.-F. Liao, Z.-G. Huang, J.-H. Wei, X.-D. Wang, H.-Y. Chen and D.-B. Kuang, Intrinsic Self-Trapped Emission in 0D Lead-Free $(C_4H_{14}N_2)_2In_2Br_{10}$ Single Crystal, *Angew. Chem., Int. Ed.*, 2019, **58**, 15435–15440.

53 H. Yang, Y. Zhang, J. Pan, J. Yin, O. M. Bakr and O. F. Mohammed, Room-Temperature Engineering of All-Inorganic Perovskite Nanocrsytals with Different Dimensionalities, *Chem. Mater.*, 2017, **29**, 8978–8982.

54 Y. Zhang, B. Fan, Y. Liu, H. Li, K. Deng and J. Fan, Quasi-self-trapped Frenkel-exciton near-UV luminescence with large Stokes shift in wide-bandgap Cs4PbCl6 nanocrystals, *Appl. Phys. Lett.*, 2018, **112**, 183101.

55 Y. Wang, S. Guo, H. Luo, C. Zhou, H. Lin, X. Ma, Q. Hu, M.-h. Du, B. Ma, W. Yang and X. Lü, Reaching 90% Photoluminescence Quantum Yield in One-Dimensional Metal Halide C4N2H14PbBr4 by Pressure-Suppressed Nonradiative Loss, *J. Am. Chem. Soc.*, 2020, **142**, 16001–16006.

56 Z. Tan, J. Li, C. Zhang, Z. Li, Q. Hu, Z. Xiao, T. Kamiya, H. Hosono, G. Niu, E. Lifshitz, Y. Cheng and J. Tang, Highly Efficient Blue-Emitting Bi-Doped Cs2SnCl6 Perovskite Variant: Photoluminescence Induced by Impurity Doping, *Adv. Funct. Mater.*, 2018, **28**, 1801131.

57 B. Lee, C. C. Stoumpos, N. Zhou, F. Hao, C. Malliakas, C.-Y. Yeh, T. J. Marks, M. G. Kanatzidis and R. P. H. Chang, Air-Stable Molecular Semiconducting Iodosalts for Solar Cell Applications: Cs2SnI6 as a Hole Conductor, *J. Am. Chem. Soc.*, 2014, **136**, 15379–15385.

58 M. Azam, S. Yue, R. Xu, K. Liu, K. Ren, Y. Sun, J. Liu, Z. Wang, S. Qu, Y. lei and Z. Wang, Highly efficient solar cells based on

Cl incorporated tri-cation perovskite materials, *J. Mater. Chem. A*, 2018, **6**, 13725–13734.

59 H. Zheng, L. Zhu, L. Hu, S. Yang, S. Chen, A. Alsaedi, T. Hayat, Y. Huang, X. Pan and S. Dai, Promoting perovskite crystal growth to achieve highly efficient and stable solar cells by introducing acetamide as an additive, *J. Mater. Chem. A*, 2018, **6**, 9930–9937.

60 X. Shen, Y. Zhang, S. V. Kershaw, T. Li, C. Wang, X. Zhang, W. Wang, D. Li, Y. Wang, M. Lu, L. Zhang, C. Sun, D. Zhao, G. Qin, X. Bai, W. W. Yu and A. L. Rogach, Zn-Alloyed CsPbI3 Nanocrystals for Highly Efficient Perovskite Light-Emitting Devices, *Nano Lett.*, 2019, **19**, 1552–1559.